Li *et al. J. Mater. Inf.* **2025**, *5*, 21
DOI: 10.20517/jmi.2024.87

Journal of Materials Informatics

Research Article

Open Access

Check for updates

High-throughput screening of phosphide compounds for potassium-ion conductive cathode application

Yawen Li[1], Natalia A. Kabanova[2], Vladislav A. Blatov[1,2], Junjie Wang[1,*]

[1]State Key Laboratory of Solidification Processing, Northwestern Polytechnical University, Xi'an 710072, Shaanxi, China.
[2]SCTMS, Samara State Technical University, Samara 443100, Russian Federation.

[*]**Correspondence to:** Prof. Junjie Wang, State Key Laboratory of Solidification Processing, Northwestern Polytechnical University, Youyi campus, 127 West Youyi Road, Beilin District, Xi'an 710072, Shaanxi, China. E-mail: wang.junjie@nwpu.edu.cn

How to cite this article: Li, Y.; Kabanova, N. A.; Blatov, V. A.; Wang, J. High-throughput screening of phosphide compounds for potassium-ion conductive cathode application. *J. Mater. Inf.* **2025**, *5*, 21. https://dx.doi.org/10.20517/jmi.2024.87

Received: 14 Dec 2024 **First Decision:** 13 Jan 2025 **Revised:** 26 Jan 2025 **Accepted:** 7 Feb 2025 **Published:** 11 Mar 2025

Academic Editor: Yaqiong Su **Copy Editor:** Pei-Yun Wang **Production Editor:** Pei-Yun Wang

Abstract

Cathode materials are crucial in potassium (K) batteries, directly impacting their performance and lifespan. In this study, we used a combination of geometrical-topological (GT) analysis, bond valence site energy (BVSE), Kinetic Monte Carlo (KMC), and first-principles calculations to screen potential cathode materials for K-ion batteries among inorganic phosphides. Through GT analysis, we screened 143 K- and P-containing compounds and identified 30 with two- or three-dimensional K-ion migration pathways. BVSE further narrowed down 13 compounds with K-ion migration energies below 1 eV. KMC simulations of ionic conductivity led to the selection of $K_3Cu_3P_2$ for detailed first-principles calculations. It was demonstrated that $K_3Cu_3P_2$ possesses a reversible capacity of 72.47 mAh·g^{-1}, minimal volume change (1.47%), and a charge compensation mechanism involving Cu and P. Its low migration energy barrier contributes to a high ionic diffusion coefficient and conductivity of 1.87×10^{-3} S·cm^{-1} at 25 °C, making $K_3Cu_3P_2$ a promising candidate for stable and efficient K-ion diffusion in cathode applications.

Keywords: High-throughput calculation screening, potassium batteries, cathode material, geometrical-topological approach, bond valence site energy, density functional theory

INTRODUCTION

Fossil fuels, including oil, gas, and coal, remain the dominant global energy source. However, their overuse has raised significant environmental and energy security concerns. To promote sustainable development, there is increasing momentum toward transitioning to clean energy sources such as solar, wind, and nuclear power, which can reduce greenhouse gas emissions and improve energy efficiency[1-5]. The development of electric vehicles and renewable energy technologies has garnered significant societal interest, with high-performance energy storage systems playing a key role in optimizing the use of clean energy[6-8]. Among these technologies, rechargeable batteries, particularly lithium (Li)-ion batteries, are seen as a critical solution for meeting diverse energy needs[9]. However, the limited lithium reserves pose a significant challenge[10-17]. As the demand for rechargeable batteries grows, there is an urgent need to develop sustainable alternatives that offer comparable performance to Li-ion batteries.

Compared to Li-ion batteries, sodium-ion batteries offer advantages such as greater abundance and lower cost[18]. However, their higher electrode potential [-2.71 V *vs.* standard hydrogen electrode (SHE)] leads to lower energy density and reduced energy storage performance[19-21]. Potassium (K), which shares similar physicochemical properties with lithium, is also abundant (2.09 wt%) and has a standard electrode potential (-2.93 V *vs.* SHE) close to that of lithium (-3.04 V *vs.* SHE). This similarity enables K-ion batteries to achieve high operating voltages and energy densities[22]. Replacing expensive materials such as lithium, cobalt, and copper, commonly used in Li-ion batteries, with more affordable and abundant alternatives such as potassium, iron, and aluminum can significantly lower costs while improving safety[23]. However, the larger ionic radius of potassium results in slower ion kinetics during the charging and discharging process, negatively impacting the electrochemical cycle performance and rate capability of K-ion batteries. Therefore, developing electrode materials that facilitate efficient and reversible K-ion transport is crucial[24-31]. High-throughput screening methods have emerged powerfully for accelerating the discovery and design of new materials[32,33]. K_2CdO_2, as a potential solid electrolyte, was selected from potassium oxides[34]. A topological quantum material, K_2MnS_2[35], was identified to be the most promising cathode for K-ion batteries.

Recently, several silicon phosphides have emerged as promising candidates for solid electrolytes. For example, Li_8SiP_4 and Li_2SiP_2, which are based on SiP_4 tetrahedral building blocks, have shown potential applicability[36]. The ionic conductivity of Li_8SiP_4 ranges from 1.15×10^{-6} S·cm^{-1} at 0 °C to 1.2×10^{-4} S·cm^{-1} at 75 °C, with an activation energy of 0.49 eV. Li_2SiP_2[36] exhibits a conductivity of 6.6×10^{-6} S·cm^{-1} at 75 °C. Meanwhile, $LiSi_2P_3$, which adopts a diorite structure, demonstrates favorable ion transport properties with a low activation energy of 0.07 eV[37]. Additionally, HT-$NaSi_2P_3$ exhibits a high total conductivity of up to 4×10^{-4} S·cm^{-1} at 25 °C, featuring the largest supertetrahedral entities (T5)[38]. For K-ion conductors, KSi_2P_3 displays an ionic conductivity of 1.6×10^{-4} S·cm^{-1} at 25 °C with an average activation energy of 0.20 eV[39,40]. These findings suggest that phosphides, particularly silicon-based phosphides, are promising candidates for K-ion conductors and warrant further exploration for future applications.

In this study, we performed a high-throughput screening of all phosphide compounds in the Inorganic Crystal Structure Database (ICSD; version 2022/2) for the first time (Schemed in Figure 1)[41]. Initially, we used the geometrical-topological (GT) approach to screen K- and P-containing compounds. Next, we applied the bond valence site energy (BVSE) method to analyze the locations of mobile ions and roughly estimate the migration barriers. This process identified 13 promising K-ion conductors with low migration barriers, which were then selected for further evaluation through Kinetic Monte Carlo (KMC) simulations. Finally, we used density functional theory (DFT) to model charge-discharge products and simulate half-cells, focusing on the most promising compound, $K_3Cu_3P_2$.

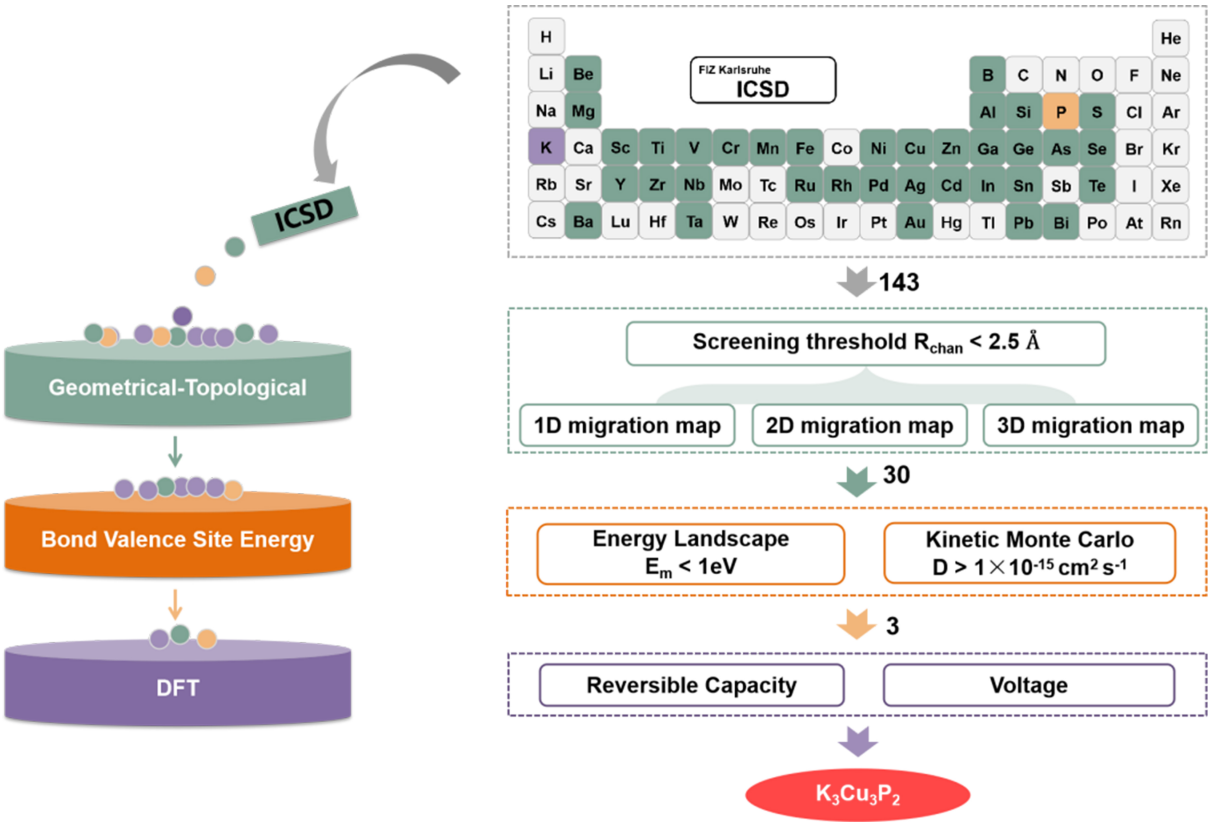

Figure 1. Workflow for screening promising potassium-ion conductors.

MATERIALS AND METHODS

GT approach

The cationic conductivity of inorganic compounds is largely governed by the presence of a continuous network of channels and voids within the crystal structure, which facilitate cation migration. In the Voronoi partition approach, the crystal space is divided into two dual subspaces: atoms and voids. To analyze cation migration pathways, the vertices and edges of Voronoi polyhedra are treated as elementary voids and channels, based on key criteria derived from known solid electrolytes. The construction of the graph and polyhedral representations of the void space, as well as the subsequent analysis of their GT characteristics, is implemented in the ToposPro software package[42]. This GT approach has been successfully applied to predict suitable cathode and electrolyte materials for various cations, including Li^+[43], Na^+[44], and Zn^{2+}[45].

To assess the geometric criteria for cation migration, we computed the radii of the elementary channels (r_{chan}) and compared them with the minimum threshold value, $r_{chan}(\min) = \gamma(r(K) + r(P))$, where $r(K)$ and $r(P)$ represent the Slater radii of K and P, respectively[46]. The deformation coefficient γ is a function of the characteristics of the mobile cations and framework anions. For this study, we used $\gamma = 0.8$, reflecting the large radius and high charge of the P^{3-} anion, and adopted $r_{chan}(\min) = 2.5$ Å as the minimal channel radius sufficient for potassium migration[47]. Additionally, we excluded channels that were solely surrounded by cations, regardless of their size, to investigate their impact on the overall conductivity pattern.

BVSE calculations

The BVSE approach[48], implemented in the GUI version of the softBV program[49,50], has become a widely adopted tool in crystal chemistry for investigating ionic migration pathways. This method is based on the

principle of maintaining local bond strength equilibrium, which is essential for understanding ion movement within a crystal lattice. By considering the Coulombic repulsion between the migrating ion and the ions in the crystal framework, the migration energy barriers for the ions are calculated[51]. The migration energy landscape for K^+ was computed using a Cube.file with a resolution of 0.1 and an automatically determined screening factor (f)[52].

To evaluate the dimensionality of the migration map, we determined the migration barrier energy (E_m). The most promising candidates for KMC simulations and DFT calculations were selected based on the criterion that E_m < 1 eV and the material should exhibit 2D or 3D ionic conductivity. This criterion is important because, although 1D ionic conductors can exhibit high conductivity under certain conditions, their sensitivity to defects and interfaces limits their practical applications.

KMC simulations

Ionic conductivities and diffusion coefficients were calculated using KMC simulations. For this purpose, supercells with volumes exceeding 10,000 Å^3 were simulated for 1 to 10 million KMC steps at 300 K. The KMC algorithm, implemented in the command-line version of softBV, utilizes approximate site and migration energies derived from BVSE analysis. The results were averaged over five different configurations to ensure statistical reliability. The unit cells were relaxed using the softBV force field. The ionic diffusion coefficient is a key performance indicator for cathode materials. Compounds with high ionic diffusion coefficients are characterized by continuous ion transport channels and low migration barriers[53,54].

DFT calculations

All DFT calculations[55] were performed using the projected augmented wave (PAW) method[56], implemented in the Vienna Ab initio Simulation Package (VASP)[57,58]. The Perdew-Burke-Ernzerhof (PBE) functional in the generalized gradient approximation (GGA)[59] was used to describe the exchange-correlation interactions. Structural optimization was carried out using the conjugate gradient method, with convergence thresholds of 10^{-5} eV for energy and 0.03 eV/Å for interatomic forces. A plane-wave energy cutoff of 520 eV was employed. To correct the self-interaction error and account for strong correlation effects in localized electrons, Hubbard U corrections were applied, with a U value of 5.2 eV for Cu[60]. The Ewald summation method[61] was used to screen the system during the K-ion charging process, leading to the generation of various configurations.

The formation energy diagram was constructed to identify the configuration with the lowest energy at different optimized concentrations. Stable intermediate phases were identified as those on the convex hull, while other compounds were classified as metastable or unstable. The energy above the hull (E_{hull}) for stable intermediate phases was calculated, and the maximum potassium removal capacity was determined for those phases with E_{hull} < 0.1 eV/atom, providing the reversible capacity of the candidate cathode materials. Ionic migration barriers for K^+ ions were calculated using the nudged elastic band (NEB) method[62], with input files generated via the PATHFINDER script (https://pathfinder.batterymaterials.info).

Compounds containing electrochemically active transition metals (Ti, V, Cr, Mn, Fe, Co, Ni, Cu, Nb, Mo, W) were considered as promising cathode materials. The theoretical capacity (in mAh·g^{-1}) was calculated using[63]:

$$C = \frac{nF}{3.6M} \quad (1)$$

where n is the number of electrons transferred per formula unit, M is the molar mass of the compound, and F is the Faraday constant. The electronic band gap E_g was taken from the Materials Project (https://materialsproject.org). The average voltage profile for each cathode reaction was determined using[64]:

$$V \approx \frac{E_{K_{x1}} - E_{K_{x2}} + (x2 - x1)E_K}{(x2 - x1)e} \tag{2}$$

where E_{Kx1} and E_{Kx2} are the DFT energies of the cathode at K concentrations x_1 and x_2, respectively. E_K is the total energy of a K atom in metallic potassium ($Im\bar{3}m$).

Ab initio molecular dynamics (AIMD) simulations were performed in the NVT ensemble for 50 ps with a time step of 1.0 fs[65]. A Nosé-Hoover thermostat was employed to control the system temperature. All AIMD simulations were carried out using a (2 × 2 × 1) supercell derived from the relaxed primitive unit cell, containing 96 atoms. The diffusion coefficient of K ions was modeled using the Arrhenius equation:

$$D = D_0 e^{-\frac{E_a}{k_B T}} \tag{3}$$

where D is the diffusion coefficient, D_0 is the prefactor of diffusion, k_B is the Boltzmann constant, E_a is the activation energy, and T is the temperature. The ionic conductivity was calculated from the extrapolated diffusion coefficient[66] using:

$$\sigma = \frac{c_K (q_K e)^2}{k_B T} D \tag{4}$$

where c_K is the concentration of K ions, q_K denotes the charge state of K ions, and e refers to the elementary charge.

RESULTS AND DISCUSSION

GT and BVSE analysis

For 143 compounds, the migration map was constructed using the criterion r_{chan}(min). Of these, the diffusion of K ions was predicted to be two-dimensional (2D) for nine compounds and three-dimensional (3D) for 21 compounds [Supplementary Table 1]. The compounds were classified based on their framework types, with frameworks grouped according to the same space group and similar chemical compositions. Previous studies[67] have shown that when the energy barrier E_m exceeds 1 eV, the diffusion of K ions is significantly hindered, although it may be overcome at elevated temperatures. In contrast, when the migration barrier E_m is less than 1 eV, the ion migration process becomes relatively facile.

In general, the results obtained from the GT analysis and the BVSE method are consistent, and the migration map of the same dimensionality is obtained [Figure 2]. When considering all channels with $r_{chan} > r_{chan}$ (min) for the construction of the migration map, an exception is found in K_4CdP_2[68], where the BVSE method predicts 2D migration, while the GT analysis indicates 3D migration. This compound exemplifies how geometrically accessible migration channels can still exhibit high energy barriers for diffusion. For

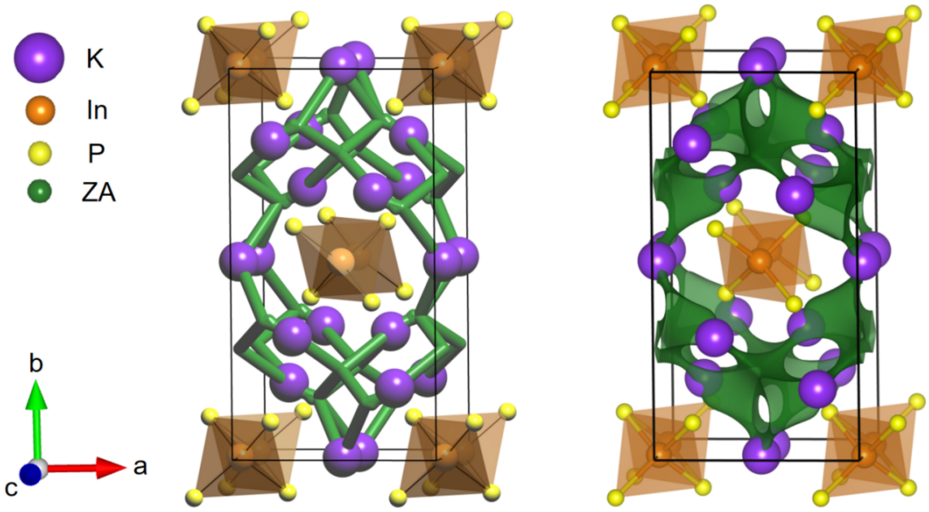

Figure 2. The crystal structures of K_3InP_2, showing the 3D potassium ionic migration map from GT approach (left) and BVSE calculation (right). Hereafter ZA designates centers of elementary voids in the GT analysis. 3D: Three-dimensional; GT: geometrical-topological; BVSE: bond valence site energy.

instance, the channels responsible for migration along the [001] direction are sufficiently wide (with r_{chan} = 3.49 Å) but are surrounded by Cd^{2+} cations [Figure 3]. The migration of K^+ ions through these channels is hindered by repulsion between K^+ and Cd^{2+} ions, a finding corroborated by the BVSE analysis. Another channel, which is also deemed inaccessible for migration according to BVSE, has two Cd^{2+} cations in its environment and a smaller radius (r_{chan} = 3.08 Å), but it does not significantly affect the overall 2D conductivity [Figure 3]. In the cases of K_4ZnP_2[69] and K_5AuP_2[70], the channels surrounded by pure cation environments - Zn and Au, respectively - have high migration energies (1.50 eV), which limits the diffusion to 2D conductivity [Supplementary Table 1]. However, in K_4BeP_2[71] and $K_3Cu_3P_2$[72], the channels surrounded by Be and Cu, respectively, exhibit much lower migration barriers (0.57-0.73 eV) and play a crucial role in facilitating conductivity, as indicated by the BVSE analysis [Supplementary Table 1].

Thirteen compounds with migration energy barriers lower than 1 eV were selected for KMC simulations at room temperature [Supplementary Table 2]. Compounds containing electrochemically active elements were considered as potential cathode materials [Table 1]. The KMC results indicate that K_2AuP[73], K_2CuP[68] and $K_3Cu_3P_2$ exhibit moderate diffusion coefficients of approximately 1×10^{-14} $cm^2 \cdot s^{-1}$, similar to the well-known lithium cathode material $LiFePO_4$[74] (10^{-14}-10^{-15} $cm^2 \cdot s^{-1}$). Based on these results, K_2AuP, K_2CuP and $K_3Cu_3P_2$ were identified as the most promising candidates for cathode materials.

Among all the phosphides considered, K_3InP_2[75] exhibits the highest ionic conductivity, approaching 1×10^{-3} $S \cdot cm^{-1}$. However, the narrow band gap of K_3InP_2 (approximately 0.75 eV) facilitates electronic conductivity, which can trigger redox reactions, potentially leading to material decomposition and affecting the long-term performance and lifespan of the battery. Note that the PBE functional exhibits a systematic underestimation in band gap predictions. According to statistical data[76], the band gaps calculated using PBE are typically 30%-50% lower than experimental values, which is attributed to the limitations of the PBE functional in describing electronic exchange and correlation energies. To mitigate this issue, the band gap of K_3InP_2 could be widened through doping, specifically by replacing In with elements of higher electronegativity or different valency. Such doping could enhance its performance as a solid electrolyte material. Substituting In with elements such as Ga or Al may be particularly effective, as these elements

Table 1. 13 most promising K-/P-containing compounds after GT and BVSE analysis

Formula	ICSD code	Space group	Migration map (GT/BVSE)	E_m	σ (S·cm^{-1})	D (cm^2·s^{-1})	C_g (mAh/g)	E_g (eV)
K_2AuP	300201	*Cmcm*	3/3	0.45	7.01×10^{-9}	6.29×10^{-14}	175.12	0.95
K_2CuP	61082	*Cmcm*	3/3	0.68	1.38×10^{-9}	1.18×10^{-14}	310.41	1.14
$K_3Cu_3P_2$	12163	$R\bar{3}m$	3/3	0.73	2.47×10^{-9}	1.89×10^{-14}	217.42	1.29
KMnP	89593	*P4/nmm*	2/2	0.45	2.34×10^{-11}	5.25×10^{-16}	214.43	0
K_4CdP_2	61084	*C2/m*	3/2	0.32	2.77×10^{-16}	2.81×10^{-21}	324.18	0.82
K_3InP_2	300141	*Ibam*	3/3	0.48	1.06×10^{-3}	1.08×10^{-8}	SE*	0.79
K_3AlP_2	300130	$P\bar{1}$	3/3	0.58	1.01×10^{-5}	6.61×10^{-11}	SE	0.70
K_6InP_3	300147	$P\bar{1}$	3/3	0.40	4.50×10^{-6}	3.41×10^{-11}	SE	0.75
K_3P	25550	$P6_3/mmc$	3/3	0.21	1.24×10^{-6}	9.67×10^{-12}	SE	0.21
K_4P_3	64625	*Cmcm*	3/3	0.77	7.33×10^{-7}	6.18×10^{-12}	SE	0
KP	14010	$P2_12_12_1$	3/3	0.39	3.01×10^{-8}	2.72×10^{-13}	SE	1.03
K_4BeP_2	300110	$R\bar{3}m$	3/3	0.57	7.63×10^{-8}	6.04×10^{-13}	SE	1.14
K_3BP_2	300104	*C2/c*	3/3	0.87	3.89×10^{-8}	3.67×10^{-13}	SE	1.67

*Potential base for solid electrolytes. GT: Geometrical-topological; BVSE: bond valence site energy.

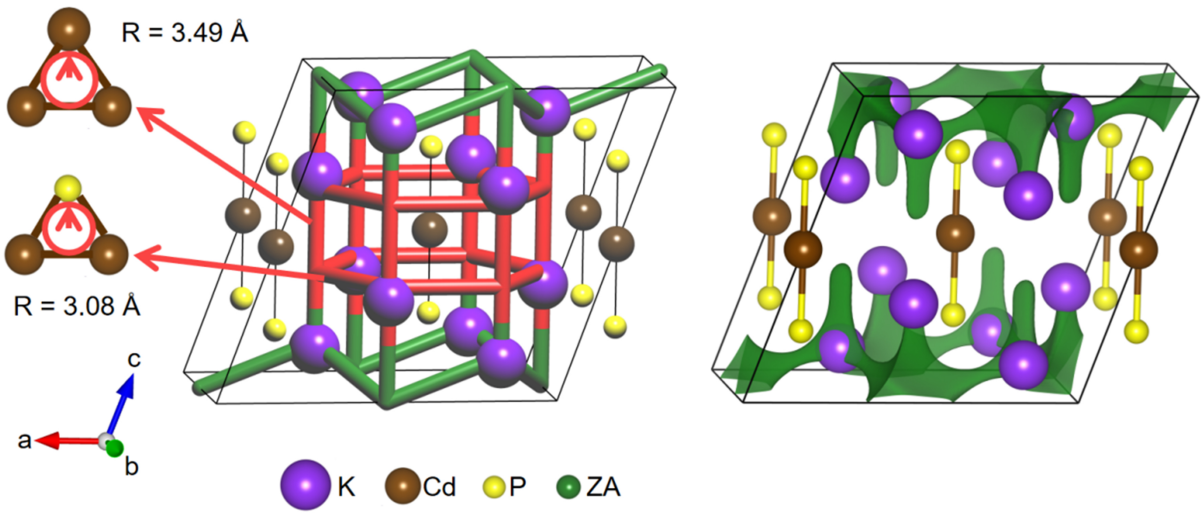

Figure 3. Crystal structures of K_4CdP_2, illustrating the 3D potassium ionic migration map (left) from the GT approach and the 2D migration map (right) derived from BVSE calculations. The relevant regions of the migration maps are highlighted in green. The elementary channels that are inaccessible to K^+ migration due to surrounding Cd^{2+} cations are highlighted in red. 3D: Three-dimensional; GT: geometrical-topological; 2D: two-dimensional; BVSE: bond valence site energy.

typically lead to a wider band gap due to their smaller atomic radii and higher electronegativities, which influence orbital overlap and the overall electronic structure. K_3InP_2 belongs to the topological type 4^3,8T23, where 4-coordinated cations (K^+ and In^{3+}) are connected to 8-coordinated P^{3-} anions. According to the TopCryst system[77], five other compounds - Na_3AlP_2[78], Na_3AlAs_2[78], Ln_2NCl_3 (Ln = La, Ce, Pr)[79] - share the same topological type and space group (*Ibam*). Notably, Na_3AlP_2 demonstrates the potential for incorporating Al^{3+} atoms into the phosphide framework of this structural motif. Na_3AlP_2 shares the same structural framework and symmetry as K_3InP_2; it possesses a wider band gap (approximately 1.35 eV), which is a key factor in its potential use for incorporating Al into the In sites of K_3InP_2, forming $K_3In_{1-x}Al_xP_2$ with an expanded band gap. This approach aligns with our goal of improving the material's performance while avoiding the redox issues observed in K_3InP_2.

DFT results

We calculated the reversible capacities of K_2AuP, K_2CuP and $K_3Cu_3P_2$. The formation energies and convex hull phase diagrams were constructed to elucidate the structural evolution during K-ion insertion and extraction. Compounds with an energy above the convex hull (E_{hull}) exceeding 0.1 eV/atom are considered thermodynamically unstable[35,80]. As shown in Figure 4, $K_3Cu_3P_2$ exhibits a reversible capacity of 72.47 mAh·g^{-1}, significantly higher than that of K_2AuP and K_2CuP.

Supplementary Figure 1 reveals that $K_3Cu_3P_2$ possesses a layered structure with the space group $R\bar{3}m$, and we constructed a 3D migration map for K ions. During the charging process, two stable intermediate compounds, $K_xCu_3P_2$ (x = 8/3, 2), were selected for analysis [Supplementary Figure 2]. We estimated the voltage for each reaction by evaluating the slope of the formation energy, revealing two primary voltage plateaus at 1.37 and 2.76 V, as shown in Figure 5A. Notably, one-third of the K ions are easily deintercalated, while the remaining ions are more challenging to extract, which influences the overall battery capacity. For comparison, the previously reported cathode material $K_2FeP_2O_7$[81] has a reversible capacity of 60 mAh·g^{-1} and a voltage plateau of around 2.7 V. In contrast, $K_3Cu_3P_2$ not only exhibits a higher reversible capacity but also a more favorable voltage profile, offering superior energy density.

During the charge/discharge cycles, K-ion insertion and extraction induce structural and volumetric changes in the cathode material. These volume changes can significantly affect the stability of the crystal structure. Large expansions or contractions can cause stress concentration within the lattice, leading to potential cracks or structural failure. As shown in Figure 5B, we analyzed the structural evolution of $K_xCu_3P_2$ (x = 3, 8/3, 2). After the extraction of one-third of the K ions, the material experienced only a slight volume reduction of 1.47%, with minimal changes in lattice constants and angles, indicating exceptional structural stability [Supplementary Figure 3]. This suggests that $K_3Cu_3P_2$ can maintain excellent reversibility and high capacity even after multiple charge-discharge cycles.

We performed a comprehensive analysis of the electronic structure of $K_xCu_3P_2$ (x = 3, 8/3, 2) by examining the density of states (DOS). $K_3Cu_3P_2$ is identified as a semiconductor, with a significant overlap between the 3*d* orbitals of Cu and the 3*p* orbitals of P, indicating a strong covalent interaction between Cu and P atoms. Upon the release of potassium atoms, some Cu^+ ions in $K_xCu_3P_2$ further undergo oxidation to Cu^{2+}, resulting in a rightward shift in the DOS and a filling of the conduction band. This shift enhances the metallic characteristics of $K_xCu_3P_2$ [Figure 6]. As an intermediate compound, $K_{7/3}Cu_3P_2$ exhibits improved electronic conductivity compared to $K_3Cu_3P_2$ [Supplementary Figure 4]. Furthermore, the increasing DOS near the Fermi level suggests that the release of potassium atoms further enhances the electronic conductivity of $K_xCu_3P_2$, which in turn improves the high-rate charging performance of the material.

To further investigate the electronic behavior, we conducted Bader charge analysis[82] to calculate the charge distribution of each atom in $K_xCu_3P_2$. As summarized in Supplementary Table 3, upon the release of 2/3 potassium atoms, the Cu and P atoms lose 0.089 and 0.064 electrons, respectively, which provides additional evidence for the contribution of Cu and P to charge compensation during ion migration.

Next, we examined the migration behavior of K ions, since migration energy barriers are critical in determining the charge and discharge rates of batteries, especially at high discharge currents, which can lead to rapid capacity fading. We identified two distinct diffusion pathways using the PATHFINDER script, and calculated the migration barriers through the CI-NEB method[83]. Path 1 involves K ion migration within the (001) plane, suggesting a 2D migration mechanism, while Path 2 follows the [001] direction, indicating a 3D migration pathway in Figure 7A. The calculated migration barriers for these two paths are 0.108 and

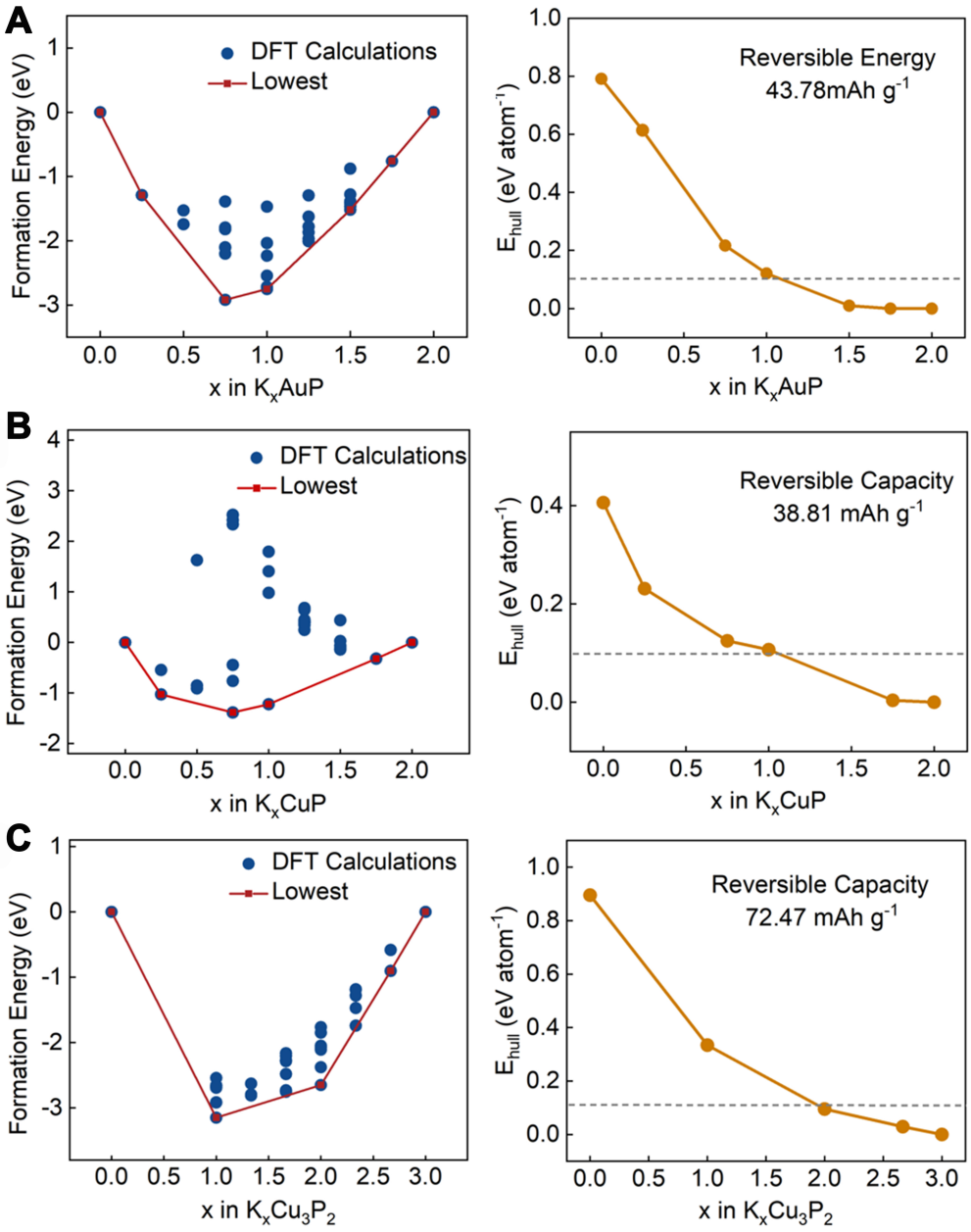

Figure 4. Formation energies during charge and discharge, along with the energy above the convex hull (E_{hull}) for different compositions of (A) K_2AuP, (B) K_2CuP and (C) $K_3Cu_3P_2$.

0.112 eV [Figure 7B], respectively, both of which are significantly lower than the results obtained from the BVSE analysis [Supplementary Table 1]. This discrepancy arises because the BVSE method does not account for lattice effects or structural transformations during cation migration[32]. For instance, previous studies on Li^+ ions have shown that BVSE tends to overestimate the migration barrier compared to DFT by a significant margin (more than twice)[84]. In contrast, the migration barriers computed by both methods for Mg^{2+} exhibit close agreement[85]. Additionally, the correlation may be influenced by computational factors such as the choice of BVSE screening factor, the DFT functional, and the basis set employed in the calculations. However, the relative values of migration barriers computed for a series of compounds by BVSE and DFT are consistent, which allows one to use BVSE for the preliminary screening of prospective

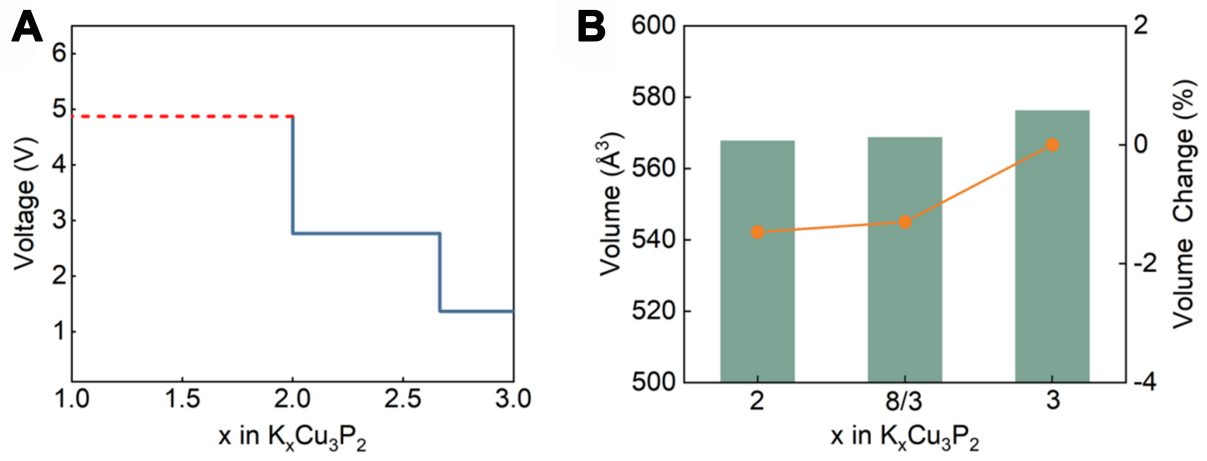

Figure 5. (A) Calculated voltages and (B) calculated changes in the unit cell volume. The dotted line indicates that this voltage plateau is difficult to achieve with conventional electrolytes.

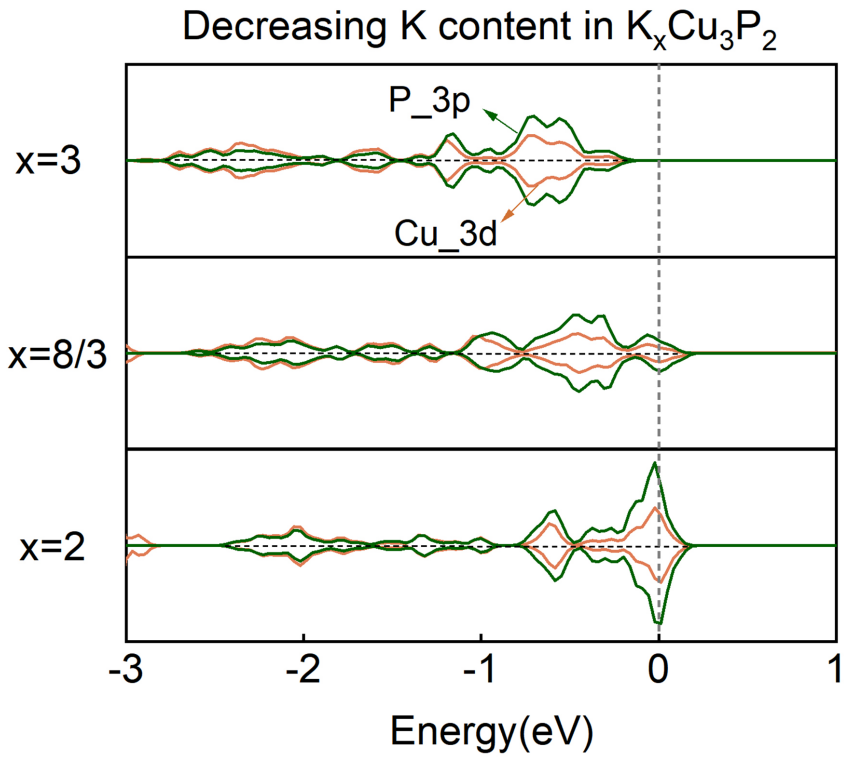

Figure 6. Calculated partial DOS for $K_xCu_3P_2$ (x = 3, 8/3, 2) with decreasing potassium content. DOS: density of states.

ionic conductors[41]. The low migration energy barriers of $K_3Cu_3P_2$ indicate a high ionic diffusion coefficient, which is beneficial for fast ion transport.

To estimate the overall K-ion migration activation energy and diffusion coefficient of the material at room temperature, we conducted AIMD simulations at temperatures ranging from 600 to 1,000 K. As shown in Figure 8A, the migration channel diagram obtained by AIMD is similar to that computed by CI-NEB. The activation energy barrier for K^+ migration was found to be 0.11 ± 0.01 eV in Figure 8B, which is in good

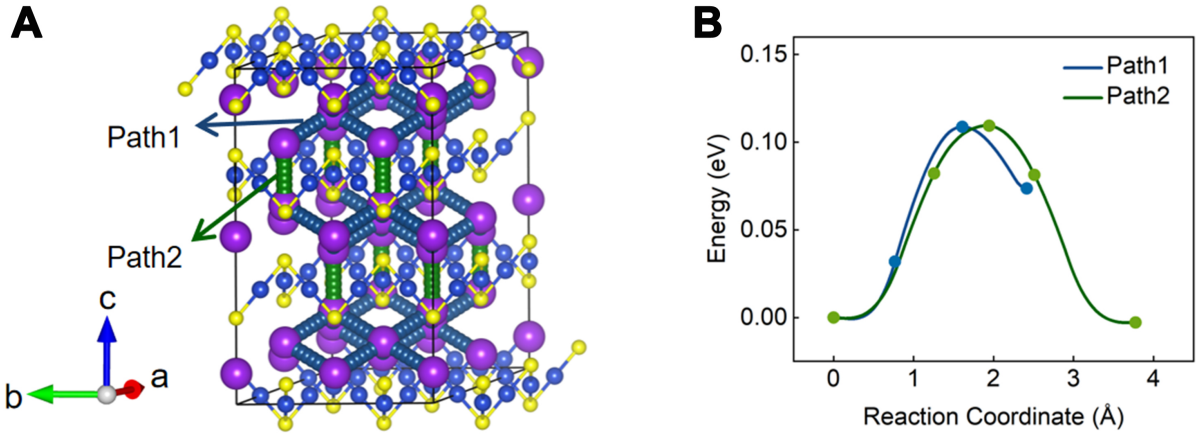

Figure 7. Illustration of (A) the migration pathways and (B) the calculated migration energy barriers for Path 1 and Path 2 in $K_3Cu_3P_2$.

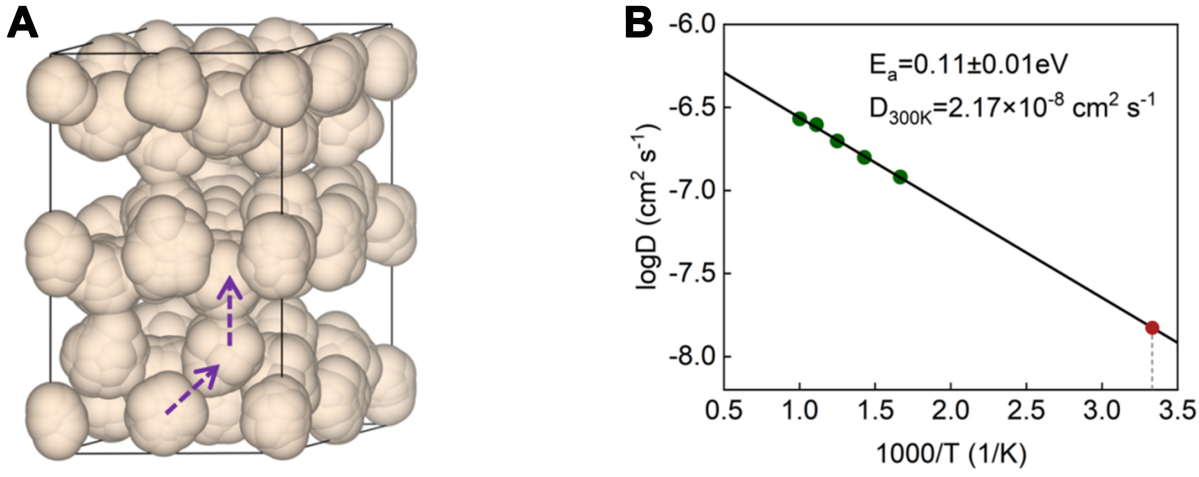

Figure 8. Illustration of (A) migration channel and (B) Arrhenius plot of the logarithm of the diffusivity, log (D), *vs.* 1000/T for $K_3Cu_3P_2$.

agreement with the value obtained from the CI-NEB calculations, confirming that the material undergoes minimal structural reorganization or phase transition during ionic migration. Based on the AIMD results, we can analyze the ion diffusion behavior during the charging process. The potassium atoms in $K_3Cu_3P_2$ are located at K1 and K2 sites, respectively. The diffusion coefficients of both ions were calculated at 600 K [Supplementary Figure 5]. According to the reversible capacity calculation [Supplementary Figure 2], the ion configuration obtained by extracting potassium from the K2 site is the most stable. The ion diffusion coefficient at the K2 site (1.43×10^{-7} cm^2·s^{-1}) is larger than that at the K1 site (4.45×10^{-8} cm^2·s^{-1}). Therefore, during the charging process, K ions at the K2 site are more likely to diffuse, contributing to the capacity.

The corresponding K-ion diffusion coefficient (D) at 300 K is calculated to be approximately 2.17×10^{-8} cm^2·s^{-1}, which is significantly higher than that of $LiFePO_4$ (10^{-14}-10^{-15} cm^2·s^{-1}). The potassium ionic conductivity, calculated using Equation (4), is about 1.87×10^{-3} S·cm^{-1} at 25 °C, which is also greater than that of KSi_2P_3 (1.6×10^{-4} S·cm^{-1} at 25 °C)[39].

CONCLUSIONS

In this study, we present a novel approach for screening phosphide compounds as potential cathode materials for K-ion batteries. Using a combination of GT analysis, BVSE calculations, KMC simulations, and DFT calculations, we have identified several promising candidates. The GT analysis revealed 30 previously unreported ionic conductors, while BVSE and KMC simulations highlighted 13 potential K-ion conductors. Among these, $K_3Cu_3P_2$ emerged as the most promising cathode material, with a diffusion coefficient exceeding 1×10^{-14} $cm^2 \cdot s^{-1}$ and a theoretical capacity of 217.42 $mAh \cdot g^{-1}$. DFT calculations further assessed the thermodynamic stability of $K_3Cu_3P_2$ by evaluating its formation energy and energy above the convex hull and predicting its reaction voltage platform. It is confirmed by DFT calculations that $K_3Cu_3P_2$ exhibits a reversible capacity of 72.47 $mAh \cdot g^{-1}$ and a voltage platform of 2.76 V, outperforming the previously reported $K_2FeP_2O_7$. Notably, this $K_3Cu_3P_2$ compound demonstrates excellent structural stability, with a minimal volume change of only 1.47% during charge-discharge cycling. Additionally, $K_3Cu_3P_2$ benefits from enhanced electronic conductivity, which facilitates high-speed charging. Its low activation energy of 0.11 eV, high diffusion coefficient of 2.17×10^{-8} $cm^2 \cdot s^{-1}$, and high conductivity of 1.87×10^{-3} $S \cdot cm^{-1}$ at 25 °C collectively contribute to improving the battery's power density. Overall, this study highlights $K_3Cu_3P_2$, discovered through our screening process, as a highly promising cathode material for K-ion batteries. It also represents an innovative step in exploring phosphides for advanced cathode applications in energy storage technologies.

DECLARATIONS

Authors' contributions

Methodology, validation, formal analysis and data curation: Li, Y.; Kabanova, N. A.
Investigation, write-review and editing and visualization: Wang, J.; Blatov, V. A.

Availability of data and materials

The data supporting the findings of this study are included in the Supplementary Materials.

Financial support and sponsorship

This work is supported by the National Natural Science Foundation of China (Grant No. 52272307), the National Key Research and Development Program of Intergovernmental Cooperation in Science and Technology (Grant No.2022YFE0141100), and the Fundamental Research Funds for the Central Universities.

Conflicts of interest

All authors declared that there are no conflicts of interest.

Ethical approval and consent to participate

Not applicable.

Consent for publication

Not applicable.

REFERENCES

1. Zhao, Z. H.; Wang, H.; Li, J.; et al. Photocatalytic acetylene hydrochlorination by pairing proton reduction and chlorine oxidation over g-C_3N_4/BiOCl catalysts. *J. Am. Chem. Soc.* **2024**, *146*, 29441-9. DOI

2. Zhang, L.; Bai, R.; Lin, J.; et al. Deprotonated 2-thiolimidazole serves as a metal-free electrocatalyst for selective acetylene hydrogenation. *Nat. Chem.* **2024**, *16*, 893-900. DOI
3. An, S.; Zhao, Z. H.; Bu, J.; et al. Multi-functional formaldehyde-nitrate batteries for wastewater refining, electricity generation, and production of ammonia and formate. *Angew. Chem. Int. Ed. Engl.* **2024**, *63*, e202318989. DOI
4. Bu, J.; Chang, S.; Li, J.; et al. Highly selective electrocatalytic alkynol semi-hydrogenation for continuous production of alkenols. *Nat. Commun.* **2023**, *14*, 1533. DOI PubMed PMC
5. Bu, J.; Liu, Z.; Ma, W.; et al. Selective electrocatalytic semihydrogenation of acetylene impurities for the production of polymer-grade ethylene. *Nat. Catal.* **2021**, *4*, 557-64. DOI
6. Goodenough, J. B.; Park, K. S. The Li-ion rechargeable battery: a perspective. *J. Am. Chem. Soc.* **2013**, *135*, 1167-76. DOI PubMed
7. Chen, Y.; Kang, Y.; Zhao, Y.; et al. A review of lithium-ion battery safety concerns: the issues, strategies, and testing standards. *J. Energy. Chem.* **2021**, *59*, 83-99. DOI
8. Xiao, J.; Shi, F.; Glossmann, T.; Burnett, C.; Liu, Z. From laboratory innovations to materials manufacturing for lithium-based batteries. *Nat. Energy.* **2023**, *8*, 329-39. DOI
9. Yuan, K.; Tu, T.; Shen, C.; et al. Self-ball milling strategy to construct high-entropy oxide coated $LiNi_{0.8}Co_{0.1}Mn_{0.1}O_2$ with enhanced electrochemical performance. *J. Adv. Ceram.* **2022**, *11*, 882-92. DOI
10. Ding, X.; Zhou, Q.; Li, X.; Xiong, X. Fast-charging anodes for lithium ion batteries: progress and challenges. *Chem. Commun.* **2024**, *60*, 2472-88. DOI PubMed
11. Kou, P.; Zhang, Z.; Wang, Z.; et al. Opportunities and challenges of layered lithium-rich manganese-based cathode materials for high energy density lithium-ion batteries. *Energy. Fuels.* **2023**, *37*, 18243-65. DOI
12. Miao, N.; Gong, Y.; Zhang, H.; et al. Discovery of two-dimensional hexagonal MBene HfBO and exploration on its potential for lithium-ion storage. *Angew. Chem. Int. Ed. Engl.* **2023**, *62*, e202308436. DOI
13. Miao, N.; Yan, Y.; Wang, J. A rising layered boride family for energy and catalysis applications: novel hexagonal MAB phases and MBenes. *ChemSusChem* **2024**, *17*, e202400229. DOI
14. Shen, Q.; He, Y.; Wang, J. Biomass-derived two-dimensional N,O-doped carbon with embedded binary-metal nanoparticles enables dendrite-free potassium-metal anodes. *J. Mater. Chem. A.* **2023**, *11*, 9829-39. DOI
15. Wang, J.; Ye, T. N.; Gong, Y.; et al. Discovery of hexagonal ternary phase Ti_2InB_2 and its evolution to layered boride TiB. *Nat. Commun.* **2019**, *10*, 2284. DOI PubMed PMC
16. Shen, Q.; Shi, Y.; He, Y.; Wang, J. Defect engineering of hexagonal MAB phase Ti_2InB_2 as anode of lithium-ion battery with excellent cycling stability. *Adv. Sci.* **2024**, *11*, e2308589. DOI PubMed PMC
17. Miao, N.; Wang, J.; Gong, Y.; et al. Computational prediction of boron-based MAX phases and MXene derivatives. *Chem. Mater.* **2020**, *32*, 6947-57. DOI
18. Jang, I.; Go, W.; Song, B.; Park, H.; Kang, Y. C.; Chun, J. Improving ionic conductivity of von-Alpen-type NASICON ceramic electrolytes via magnesium doping. *J. Adv. Ceram.* **2023**, *12*, 1058-66. DOI
19. Liu, M.; Wu, F.; Gong, Y.; et al. Interfacial-catalysis-enabled layered and inorganic-rich SEI on hard carbon anodes in ester electrolytes for sodium-ion batteries. *Adv. Mater.* **2023**, *35*, e2300002. DOI
20. Kate, R. S.; Jadhav, H. S.; Chothe, U. P.; et al. Critical review of the recent progress and challenges of polyanion $Na_3V_2(PO_4)_3$ cathode materials in rechargeable sodium-ion batteries. *J. Mater. Chem. A.* **2024**, *12*, 7418-51. DOI
21. Wang, L.; Tian, H.; Yao, X.; Cai, Y.; Gao, Z.; Su, Z. Research progress and modification measures of anode and cathode materials for sodium-ion batteries. *ChemElectroChem* **2024**, *11*, e202300414. DOI
22. Eftekhari, A.; Jian, Z.; Ji, X. Potassium secondary batteries. *ACS. Appl. Mater. Interfaces.* **2017**, *9*, 4404-19. DOI PubMed
23. Zhang, W.; Liu, Y.; Guo, Z. Approaching high-performance potassium-ion batteries via advanced design strategies and engineering. *Sci. Adv.* **2019**, *5*, eaav7412. DOI PubMed PMC
24. Han, J.; Li, G. N.; Liu, F.; et al. Investigation of $K_3V_2(PO_4)_3$/C nanocomposites as high-potential cathode materials for potassium-ion batteries. *Chem. Commun.* **2017**, *53*, 1805-8. DOI
25. Chihara, K.; Katogi, A.; Kubota, K.; Komaba, S. $KVPO_4F$ and $KVOPO_4$ toward 4 volt-class potassium-ion batteries. *Chem. Commun.* **2017**, *53*, 5208-11. DOI
26. Kim, H.; Seo, D. H.; Kim, J. C.; et al. Investigation of potassium storage in layered P3-type $K_{0.5}MnO_2$ cathode. *Adv. Mater.* **2017**, 29. DOI
27. Kim, H.; Kim, J. C.; Bo, S.; Shi, T.; Kwon, D.; Ceder, G. K-ion batteries based on a P2-type $K_{0.6}CoO_2$ cathode. *Adv. Energy. Mater.* **2017**, *7*, 1700098. DOI
28. Yang, Z.; Li, W.; Zhang, G.; et al. Constructing Sb-O-C bond to improve the alloying reaction reversibility of free-standing Sb_2Se_3 nanorods for potassium-ion batteries. *Nano. Energy.* **2022**, *93*, 106764. DOI
29. Li, W.; Yang, Z.; Zuo, J.; Wang, J.; Li, X. Emerging carbon-based flexible anodes for potassium-ion batteries: progress and opportunities. *Front. Chem.* **2022**, *10*, 1002540. DOI PubMed PMC
30. Kim, H.; Kim, J. C. Opportunities and challenges in cathode development for non-lithium-ion batteries. *eScience* **2024**, *4*, 100232. DOI
31. Liu, X.; Chu, J.; Wang, Z.; et al. Design and optimization of carbon materials as anodes for advanced potassium-ion storage. *Rare. Met.* **2024**, *43*, 5516-48. DOI
32. Jonderian, A.; Jia, S.; Yoon, G.; et al. Accelerated development of high voltage Li-ion cathodes. *Adv. Energy. Mater.* **2022**, *12*,

2201704. DOI

33. Guo, X.; Wang, Z.; Yang, J.; Gong, X. Machine-learning assisted high-throughput discovery of solid-state electrolytes for Li-ion batteries. *J. Mater. Chem. A.* **2024**, *12*, 10124-36. DOI
34. Xiao, R.; Li, H.; Chen, L. High-throughput computational discovery of K_2CdO_2 as an ion conductor for solid-state potassium-ion batteries. *J. Mater. Chem. A.* **2020**, *8*, 5157-62. DOI
35. Wang, Y.; Liu, J.; Du, P.; Sun, Z.; Sun, Q. Screening topological quantum cathode materials for K-ion batteries by graph neural network and first-principles calculations. *ACS. Appl. Energy. Mater.* **2023**, *6*, 4503-10. DOI
36. Toffoletti, L.; Kirchhain, H.; Landesfeind, J.; et al. Lithium ion mobility in lithium phosphidosilicates: crystal structure, ^{7}Li, ^{29}Si, and ^{31}P MAS NMR spectroscopy, and impedance spectroscopy of Li_8SiP_4 and Li_2SiP_2. *Chemistry* **2016**, *22*, 17635-45. DOI
37. Haffner, A.; Bräuniger, T.; Johrendt, D. Supertetrahedral networks and lithium-ion mobility in Li_2SiP_2 and $LiSi_2P_3$. *Angew. Chem. Int. Ed. Engl.* **2016**, *55*, 13585-8. DOI
38. Haffner, A.; Hatz, A. K.; Moudrakovski, I.; Lotsch, B. V.; Johrendt, D. Fast sodium-ion conductivity in supertetrahedral phosphidosilicates. *Angew. Chem. Int. Ed. Engl.* **2018**, *57*, 6155-60. DOI PubMed
39. Haffner, A.; Hatz, A. K.; Zeman, O. E. O.; Hoch, C.; Lotsch, B. V.; Johrendt, D. Polymorphism and fast potassium-ion conduction in the T5 supertetrahedral phosphidosilicate KSi_2P_3. *Angew. Chem. Int. Ed. Engl.* **2021**, *60*, 13641-6. DOI PubMed PMC
40. Zhang, Z.; Guo, J.; Sun, S.; et al. Optimized valence state of Co and Ni in high-entropy alloy for high active-stable OER. *Rare. Met.* **2023**, *42*, 3607-13. DOI
41. Kabanov, A. A.; Morkhova, Y. A.; Bezuglov, I. A.; Blatov, V. A. 7.13 - Computational design of materials for metal-ion batteries. In: Comprehensive inorganic chemistry III. Elsevier; 2023. pp. 404-29. DOI
42. Blatov, V. A.; Shevchenko, A. P.; Proserpio, D. M. Applied topological analysis of crystal structures with the program package ToposPro. *Cryst. Growth. Des.* **2014**, *14*, 3576-86. DOI
43. Anurova, N.; Blatov, V.; Ilyushin, G.; Blatova, O.; Ivanovschitz, A.; Demyanets, L. Migration maps of Li^+ cations in oxygen-containing compounds. *Solid. State. Ionics.* **2008**, *179*, 2248-54. DOI
44. Meutzner, F.; Münchgesang, W.; Kabanova, N. A.; et al. On the way to new possible Na-ion conductors: the voronoi-dirichlet approach, data mining and symmetry considerations in ternary Na oxides. *Chemistry* **2015**, *21*, 16601-8. DOI
45. Morkhova, Y. A.; Rothenberger, M.; Leisegang, T.; Adams, S.; Blatov, V. A.; Kabanov, A. A. Computational search for novel Zn-ion conductors - a crystallochemical, bond valence, and density functional study. *J. Phys. Chem. C.* **2021**, *125*, 17590-9. DOI
46. Slater, J. C. Atomic radii in crystals. *J. Chem. Phys.* **1964**, *41*, 3199-204. DOI
47. Shannon, R. D.; Kabanova, N. A.; Fischer, R. X. Empirical electronic polarizabilities: deviations from the additivity rule. II. Structures exhibiting ion conductivity. *Cryst. Res. Technol.* **2019**, *54*, 1900037. DOI
48. Chen, H.; Adams, S. Bond softness sensitive bond-valence parameters for crystal structure plausibility tests. *IUCrJ* **2017**, *4*, 614-25. DOI PubMed PMC
49. Chen, H.; Wong, L. L.; Adams, S. SoftBV - a software tool for screening the materials genome of inorganic fast ion conductors. *Acta. Crystallogr. B. Struct. Sci. Cryst. Eng. Mater.* **2019**, *75*, 18-33. DOI PubMed
50. Wong, L. L.; Phuah, K. C.; Dai, R.; Chen, H.; Chew, W. S.; Adams, S. Bond valence pathway analyzer - an automatic rapid screening tool for fast ion conductors within softBV. *Chem. Mater.* **2021**, *33*, 625-41. DOI
51. He, B.; Mi, P.; Ye, A.; et al. A highly efficient and informative method to identify ion transport networks in fast ion conductors. *Acta. Mater.* **2021**, *203*, 116490. DOI
52. Wong, L. L.; Chen, H.; Adams, S. Design of fast ion conducting cathode materials for grid-scale sodium-ion batteries. *Phys. Chem. Chem. Phys.* **2017**, *19*, 7506-23. DOI PubMed
53. Chung, S. Y.; Bloking, J. T.; Chiang, Y. M. Electronically conductive phospho-olivines as lithium storage electrodes. *Nat. Mater.* **2002**, *1*, 123-8. DOI PubMed
54. Gu, W.; Ezbiri, M.; Prasada, R. R.; Avdeev, M.; Adams, S. Effects of penta- and trivalent dopants on structure and conductivity of $Li_7La_3Zr_2O_{12}$. *Solid. State. Ionics.* **2015**, *274*, 100-5. DOI
55. Hohenberg, P.; Kohn, W. Inhomogeneous electron gas. *Phys. Rev.* **1964**, *136*, B864-71. DOI
56. Blöchl, P. E. Projector augmented-wave method. *Phys. Rev. B. Condens. Matter.* **1994**, *50*, 17953-79. DOI PubMed
57. Kresse, G.; Furthmüller, J. Efficient iterative schemes for ab initio total-energy calculations using a plane-wave basis set. *Phys. Rev. B. Condens. Matter.* **1996**, *54*, 11169-86. DOI PubMed
58. Wang, V.; Xu, N.; Liu, J.; Tang, G.; Geng, W. VASPKIT: a user-friendly interface facilitating high-throughput computing and analysis using VASP code. *Comput. Phys. Commun.* **2021**, *267*, 108033. DOI
59. Perdew, J. P.; Burke, K.; Ernzerhof, M. Generalized gradient approximation made simple. *Phys. Rev. Lett.* **1996**, *77*, 3865-8. DOI PubMed
60. Lalroliana, B.; Lalmuanchhana; Lalhriatzuala DFT + U study of electronic and optical properties of Cu_3TMTe_4: TM = V, Nb, Ta with incorporation of SOC. *Mater. Today. Proc.* **2023**, *In Press*,. DOI
61. Toukmaji, A. Y.; Board, J. A. Ewald summation techniques in perspective: a survey. *Comput. Phys. Commun.* **1996**, *95*, 73-92. DOI
62. Henkelman, G.; Jónsson, H. Improved tangent estimate in the nudged elastic band method for finding minimum energy paths and saddle points. *J. Chem. Phys.* **2000**, *113*, 9978-85. DOI
63. Tan, P.; Wei, Z.; Shyy, W.; Zhao, T. Prediction of the theoretical capacity of non-aqueous lithium-air batteries. *Appl. Energy.* **2013**, *109*, 275-82. DOI

64. Toriyama, M. Y.; Kaufman, J. L.; Van der Ven, A. Potassium ordering and structural phase stability in layered K_xCoO_2. *ACS. Appl. Energy. Mater.* **2019**, *2*, 2629-36. DOI
65. Herr, J. D.; Steele, R. P. Accelerating ab initio molecular dynamics simulations by linear prediction methods. *Chem. Phys. Lett.* **2016**, *661*, 42-7. DOI
66. Kim, J. S.; Jung, W. D.; Choi, S.; et al. Thermally induced S-sublattice transition of Li_3PS_4 for fast lithium-ion conduction. *J. Phys. Chem. Lett.* **2018**, *9*, 5592-7. DOI
67. Eremin, R.; Kabanova, N.; Morkhova, Y.; Golov, A.; Blatov, V. High-throughput search for potential potassium ion conductors: a combination of geometrical-topological and density functional theory approaches. *Solid. State. Ionics.* **2018**, *326*, 188-99. DOI
68. Eisenmann, B.; Somer, M. On new ternary alkali metal phosphides: K_2CuP, NaZnP and K_4CdP_2. *Z. Naturforsch. B.* **1985**, *40*, 1419-23. DOI
69. Eisenmann, B.; Somer, M. Intermetallic compounds with $HgCl_2$ isoelectronic anions: crystal structure and vibrational spectra of Na_4HgP_2, K_4ZnP_2, K_4CdP_2 and K_4HgP_2. *Z. Naturforsch. B.* **1989**, *44*, 1228-32. DOI
70. Eisenmann, B.; Klein, J.; Somer, M. Linear anions $[CuAs_2]^{5-}$, $[AuP_2]^{5-}$ and $[AuAs_2]^{5-}$ in potassium compounds. *J. Alloys. Compd.* **1992**, *178*, 431-9. DOI
71. Somer, M.; Hartweg, M.; Peters, K.; von Schnering, H. G. Crystal structure of tetrapotassium diphosphidoberyllate, K_4BeP_2. *Zeitschrift. für. Kristallographie.* **1990**, *192*, 263-4. DOI
72. Savelsberg, G.; Schäfer, H. On the preparation and crystal structure of K_3CU_3P. *Z. Naturforsch. B.* **1978**, *33*, 590-2. DOI
73. Eisenmann, B.; Klein, J.; Somer, M. Crystal structure of dipotassium catena-phosphidoaurate(I), K_2AuP. *Crystall. Mater.* **1991**, *197*, 277-8. DOI
74. Orikasa, Y.; Gogyo, Y.; Yamashige, H.; et al. Ionic conduction in lithium ion battery composite electrode governs cross-sectional reaction distribution. *Sci. Rep.* **2016**, *6*, 26382. DOI PubMed PMC
75. Blase, W.; Cordier, G.; Somer, M. Crystal structure of tripotassium catenadi-μ-phosphido-indate, K_3InP_2. *Zeitschrift. für. Kristallographie.* **1991**, *195*, 109-10. DOI
76. Flores, E. M.; Moreira, M. L.; Piotrowski, M. J. Structural and electronic properties of bulk ZnX (X = O, S, Se, Te), ZnF_2, and ZnO/ZnF_2: a DFT investigation within PBE, PBE + U, and hybrid HSE functionals. *J. Phys. Chem. A.* **2020**, *124*, 3778-85. DOI
77. Shevchenko, A. P.; Shabalin, A. A.; Karpukhin, I. Y.; Blatov, V. A. Topological representations of crystal structures: generation, analysis and implementation in the *TopCryst* system. *Sci. Technol. Adv. Mater. Methods.* **2022**, *2*, 250-65. DOI
78. Ohse, L.; Somer, M.; Blase, W.; Cordier, G. Compounds with SiS_2 isoelectronic anions $_\infty^1[AlX_{4/2}^{3-}]$ and $_\infty^1[InP_{4/2}^{3-}]$: synthesis, crystal structures and vibrational spectra of $Na_3[AlX_2]$, $K_2Na[AlX_2]$ and $K_3[InP_2]$ (X = P, As). *Z. Naturforsch. B.* **1993**, *48*, 1027-34. DOI
79. Schurz, C. M.; Schleid, T. Chains of trans-edge connected $[ZM_4]$ tetrahedra (Z=N and O) in the lanthanide nitride chlorides M_2NCl_3 and $Na_2M_4ONCl_9$ (M=La–Nd). *J. Alloys. Compd.* **2009**, *485*, 110-8. DOI
80. Wu, W.; Sun, Q. Screening topological quantum materials for Na-ion battery cathode. *ACS. Mater. Lett.* **2022**, *4*, 175-80. DOI
81. Hosaka, T.; Shimamura, T.; Kubota, K.; Komaba, S. Polyanionic compounds for potassium-ion batteries. *Chem. Rec.* **2019**, *19*, 735-45. DOI PubMed
82. Sanville, E.; Kenny, S. D.; Smith, R.; Henkelman, G. Improved grid-based algorithm for Bader charge allocation. *J. Comput. Chem.* **2007**, *28*, 899-908. DOI PubMed
83. Henkelman, G.; Uberuaga, B. P.; Jónsson, H. A climbing image nudged elastic band method for finding saddle points and minimum energy paths. *J. Chem. Phys.* **2000**, *113*, 9901-4. DOI
84. Ling, S.; Gao, J.; Xiao, R.; Chen, L. High-throughput theoretical design of lithium battery materials. *Chin. Phys. B.* **2016**, *25*, 018208. DOI
85. Nishitani, Y.; Adams, S.; Ichikawa, K.; Tsujita, T. Evaluation of magnesium ion migration in inorganic oxides by the bond valence site energy method. *Solid. State. Ionics.* **2018**, *315*, 111-5. DOI